

Heterogeneous Chemical State of Carbon in Fe–C Binary Alloys

Takayuki HARANO,^{1,2)*} Yuki YOSHIMOTO,¹⁾ Yasuo TAKEICHI,^{2,3)} Tomohito TANAKA,¹⁾ Eiji ODA,⁴⁾
Shunsuke TANIGUCHI,¹⁾ Daisuke WAKABAYASHI,^{2,3)} Shohei YAMASHITA,^{2,3)}
Reiko MURAO¹⁾ and Masao KIMURA^{2,3)}

1) Advanced Technology Research Laboratories, Research and Development, Nippon Steel Corporation, Futtsu, Chiba, 293-8511 Japan.

2) Department of Materials Structure Science, School of High Energy Accelerator Science, The Graduate University for Advanced Studies (SOKENDAI), Tsukuba, Ibaraki, 305-0801 Japan.

3) Photon Factory, Institute of Materials Structure Science, High Energy Accelerator Research Organization (KEK), Tsukuba, Ibaraki, 305-0801 Japan.

4) Materials Characterization Division, Futtsu Unit, Nippon Steel Technology Co., Ltd., 20-1 Shintomi, Futtsu, Chiba, 293-0011 Japan.

(Received on October 6, 2021; accepted on December 27, 2021; J-STAGE Advance published date: February 9, 2022)

In this study, we performed scanning transmission X-ray microscopy with a spatial resolution of approximately 50 nm to investigate the two-dimensional mapping of the chemical states of carbon in Fe–C alloy. The lamellar texture (pearlite) consisting of ferrite (α -Fe) and θ -Fe₃C with an interval of approximately 100 nm was identified by absorption from the carbon 1s→2p excitation in the X-ray absorption image. It was clearly observed that there exist more than two types of chemical states of carbon in θ -Fe₃C depending on the microtextures. The differences in chemical states were found between grained θ -Fe₃C and lamellar θ -Fe₃C in pearlite, which might have originated from the texture and morphology of the θ -Fe₃C. To consider the origins of the differences, we performed first-principles calculations by assuming the distortion and crystal anisotropy of the unit cell of the θ -Fe₃C structure. The results suggest that the anisotropy of the crystal structure of θ -Fe₃C and the lattice strain within lamellar θ -Fe₃C fail to explain the differences, and therefore, other factors should be considered.

KEY WORDS: Fe–C alloy; microstructural analysis; first-principles calculations; X-ray absorption; X-ray microscopy; chemical state.

1. Introduction

The mechanical properties of steel products vary with respect to their applications. Depending on the various needs, the types and number of additional elements and the heat patterns during the heating and rolling processes are controlled accordingly.¹⁾ Carbon is one of the most important elements for controlling the mechanical properties of steel; it exists in the steel microstructure as either a solid solution or segregated elements and carbides, among other types.¹⁾ Although the presence of carbon in steel has been observed by transmission electron microscopy-electron energy loss spectroscopy (TEM-EELS),²⁾ electron probe micro analysis,³⁾ and three-dimensional atom-probe tomography (APT),^{4,5)} there are few studies that focus on the chemical state of carbon (e.g., chemical bond species and bond distance) in steel.^{6–9)} Furthermore, in electron micros-

copy, hydrocarbon molecules in the measurement chamber are adsorbed onto the sample surface as a result of electron beam irradiation, which causes contamination and makes it difficult to quantify and analyze the chemical state of carbon in the samples. G. F. Bastin *et al.*¹⁰⁾ and W. Lengauer *et al.*¹¹⁾ reported that the distribution of oxygen gas can be used to cleanse sample surfaces. However, it is concerned that oxygen gas might be the origin of another contamination or damage to the sample surface and might not remove the contamination of the sample surface completely. In addition, it was difficult to evaluate the detailed chemical state of the single-phase carbide by conventional X-ray absorption spectroscopy, even if the excitation efficiency was better than that of the electron beam. This is because it is difficult to synthesize single-phase carbide and the spatial resolution of conventional X-ray absorption spectroscopy is not sufficiently high to investigate carbide in steel microstructures.

Although the spatial resolution of X-ray absorption spectroscopy is approximately 10–50 times larger than that

* Corresponding author: E-mail: harano.ya6.takayuki@jp.nipponsteel.com



of electron microscopy, it enables the investigation of the chemical state more quantitatively than electron-based techniques, such as TEM-EELS.¹²⁾ In terms of their excitation efficiency from the ground state to the excited states, X-rays are superior to electron beams for chemical state analysis.¹³⁾ In addition, it is preferable to perform chemical state mapping using X-ray absorption microscopy to investigate the case where carbon is partitioned from carbides in a solid solution with little to no crystalline content compared to diffraction measurements by electron microscopy. That is because it is difficult to reveal the local information about carbon in amorphous phases using diffraction measurements. Another merit is that X-ray absorption spectroscopy simultaneously provides the surface (where the probing depth is on the order of a few to several nanometers) and bulk (where the probing depth is the thickness of the thin film sample (approximately 80 nm in this study)) information of samples through different experimental geometries, such as transmission and conversion electron yield (CEY) methods; this is especially important in metal specimens where the surface is easily oxidized and/or contaminated with carbon.

Therefore, in this study, we focused on scanning transmission X-ray microscopy (STXM) with approximately 50 nm of spatial resolution. We obtained X-ray absorption images of the carbon *K*-edge by STXM to identify the lamellar microstructure of ferrite and θ -Fe₃C in pearlite, with an interval of approximately 100 nm. The sample in this study was one of the most suitable samples for evaluating the usefulness of chemical state mapping for carbon in steel by STXM because it consisted of multiple microstructures, such as grained carbides, the lamellar microstructure of metal (*i.e.*, a low carbon solution), and carbide (including high carbon). We also performed two-dimensional chemical state mapping of carbon on the surface (on the order of a few to several nanometers) and in bulk (with a sample thickness of approximately 80 nm) in an Fe–C alloy using the transmission method and CEY method by STXM simultaneously, to clarify the effects of surface oxidation and/or contamination. The X-ray transmittance was measured in the transmission method (see Eqs. (1) and (2)), and the conversion electron yield was measured in the CEY method (see Eq. (3)) as discussed in chapter 2.3. Thus, the probing depth of transmission method and CEY method are the thickness of thin film sample (approximately 80 nm in this study) and a few nanometers, respectively. It was revealed that the carbon *K*-edge spectra of the grained θ -Fe₃C were different from those of the lamellar θ -Fe₃C in the Fe–C alloy.

To determine the origin of this difference, we performed first-principles calculations by assuming the distortion and crystal anisotropy of the unit cell of the θ -Fe₃C structure, suggesting the anisotropy of the crystal structure of θ -Fe₃C and the lattice strain within lamellar θ -Fe₃C.

2. Experimental

2.1. Sample Preparation

The initial composition of our sample was Fe-1.48C-0.005Si-0.032Al-0.0008N (mass%); its final composition after heat treatment was similar to the initial composition. The sample was prepared by the vacuum melting method. As shown in **Fig. 1**, the sample was dissolved in a N₂ atmosphere at atmospheric pressure, rolled to a size of 220 × 100 × 1.6 mm (*i.e.*, width × length × height), heat-treated at 900°C for 4 min, and water-cooled. Subsequently, the sample was further tempered at 400°C for 10 min and cooled in the furnace; it had a pearlite microstructure, which is a lamellar microstructure composed of ferrite and θ -Fe₃C. Moreover, for the TEM and STXM observations, a thin sample of approximately 10 μ m × 10 μ m × 100 nm was prepared by focused ion beam (FIB) processing, while the surface layer damaged by this processing was removed by argon milling. Finally, the sample thickness was adjusted to approximately 80 nm.

2.2. Electron Diffraction Measurements

To confirm the crystal structure of the generated crystal phases in the sample, we performed electron diffraction measurements using TEM at various sample positions, as shown in **Figs. 2(a)** to **2(d)**, in which (a), (b), and (c) correspond to points in the grained θ -Fe₃C, whereas (d) corresponds to a point in the lamellar θ -Fe₃C. The electron beam diffraction patterns of the sample positions in **Figs. 2(a)** to

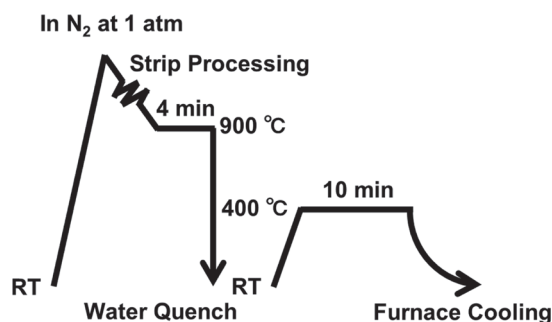


Fig. 1. Heat pattern conditions of the sample.

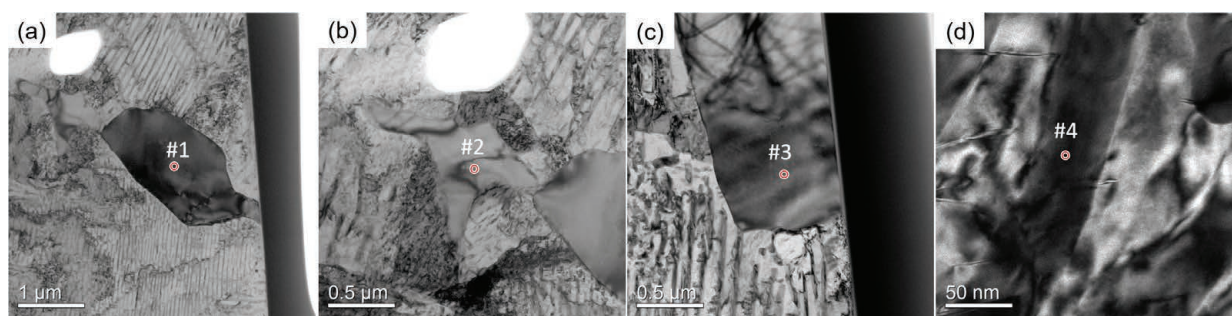


Fig. 2. TEM images of (a), (b), and (c) grained θ -Fe₃C and (d) lamellar θ -Fe₃C in the sample. (Online version in color.)

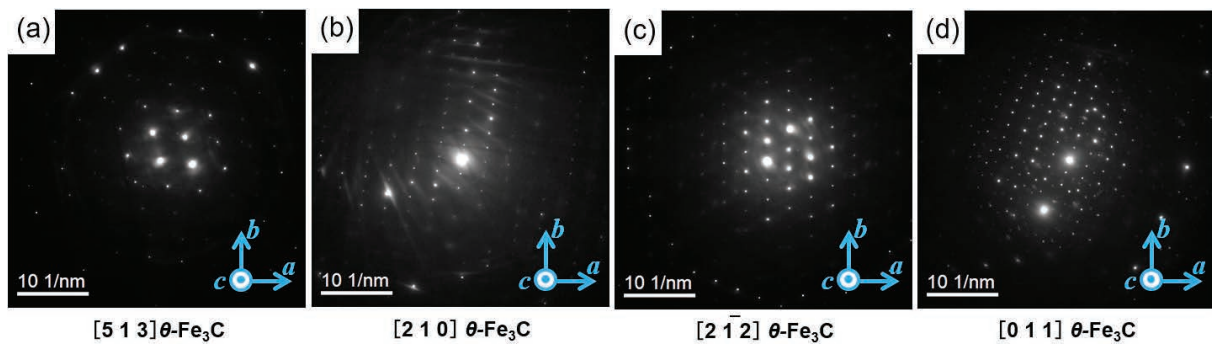


Fig. 3. Electron diffraction images at points #1–4 in Figs. 2(a) to 2(d). (Online version in color.)

Table 1. Euler angles (Φ , θ , Ψ) of θ -Fe₃C at each sample position (i.e., #1–4) in Fig. 2. The Cartesian coordinate system that serves as the reference for rotation is the coordinate system shown in Fig. 3.

| | Φ (degree) | θ (degree) | Ψ (degree) |
|----|-----------------|-------------------|-----------------|
| #1 | -112.0 | 62.7 | 75.2 |
| #2 | -6.0 | 90.0 | 56.5 |
| #3 | -21.0 | 126.0 | 56.5 |
| #4 | -110.0 | 56.1 | 0.0 |

2(d) are illustrated in Fig. 3(a) to 3(d), respectively, which suggested that the crystal orientations along the normal direction of the surface of the thin film sample at points in Figs. 2(a) to 2(d) were [513], [210], [2 $\bar{1}$ 2], and [011], respectively. The Euler angles (Φ , θ , Ψ) that reproduce each unit cell position at #1–4 in Fig. 2 are presented in Table 1, in which, Φ , θ , and Ψ indicate the rotation angles around the a , b , and c axes of the Cartesian coordinate in Fig. 3, respectively. The θ/Φ directions were rotated by 5.0°/1.0°, 5.0°/1.0°, 5.0°/5.0°, and 8.0°/3.0° before measuring the diffraction pattern at positions #1–4, respectively, to obtain lower diffraction patterns of θ -Fe₃C, which made it easier to determine the crystal orientation of θ -Fe₃C parallel to that of the incident X-ray. The direction of lamination was not uniform, while the thickness of the thin film sample was less than approximately 100 nm. As described above, the grained particles in this sample consisted of θ -Fe₃C and the constituents of the lamellar microstructure were confirmed to be ferrite and θ -Fe₃C.

2.3. STXM Measurements

The STXM measurements were performed using a compact scanning transmission X-ray microscopy (cSTXM)¹⁴ at BL-13A of Photon Factory; this enabled us to obtain the X-ray absorption spectra using the transmission and CEY methods simultaneously with a spatial resolution of approximately 50 nm. A schematic of the optical system of the cSTXM is demonstrated in Fig. 4. The X-ray beam was focused at approximately 50 nm using a Fresnel zone plate (FZP). In the experiment, the inside of the measurement chamber had a helium atmosphere of 1.0×10^4 Pa to maintain good thermal conductivity. The details of each measurement method¹⁵ are described below. In the transmission method, the X-ray absorption ratios before and after transmission through a thin sample were measured with a

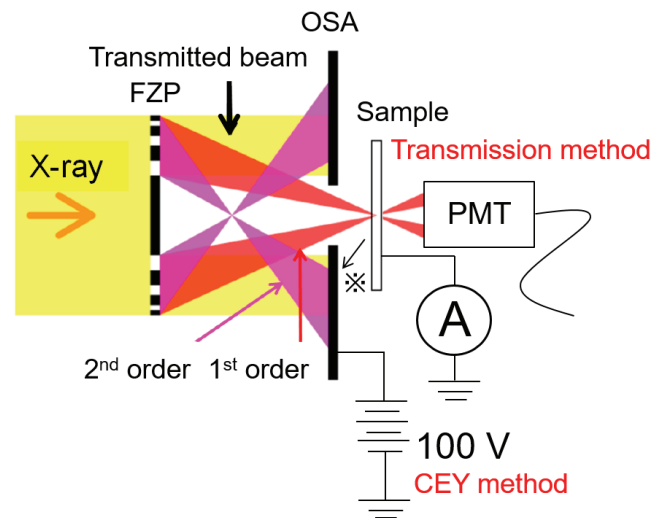


Fig. 4. Schematic diagrams of transmission method and CEY method in cSTXM. Refer to the text for the abbreviations. (Online version in color.)

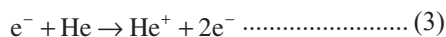
photomultiplier tube. The signal detected by the transmission method included information on the linear absorption coefficient and the thickness of the sample. Assuming that the X-ray absorption intensities before and after the transmission were $I_0(E)$ and $I(E)$, respectively, their relationship was expressed as Eq. (1), where $\mu(E)$ is the linear absorption coefficient and t is the sample thickness. The energy dependence of the optical density (OD) was obtained as shown in Eq. (2), which is the product of the linear absorption coefficient and sample thickness. $I_0(E)$ is the X-ray absorption intensity of X-rays that directly enter the detector without passing through the sample during measurement.

$$I(E) = I_0(E)e^{-\mu(E)t} \quad (1)$$

$$OD \equiv \mu(E)t = \ln \frac{I_0(E)}{I(E)} \quad (2)$$

On the other hand, the principle of the CEY method is based on the fact that the X-ray absorption intensity is proportional to the number of Auger electrons. When the sample was irradiated with X-rays, Auger electrons generated from the sample surface and secondary electrons that collided with helium atoms in the cSTXM chamber were detected as the sample current by applying a voltage to the order-sorting aperture (OSA), which was installed upstream of the sample to allow only the first-order diffracted light

from the FZP to pass. The collision process of photoelectrons and helium atoms, marked as \otimes in Fig. 4, is a reaction expressed as in Eq. (3).



During CEY-based measurements, electrons are detected by applying a voltage of 100 V. This method is sensitive to the surface state of the sample because the electrons that escape from the surface are within approximately 2–3 nm of the surface.¹⁶⁾ The signal intensity of CEY is proportional to the intensity ratio of the X-ray $I_0(E)$ before irradiation and the detected current $i(E)$ after passing through the sample, and is expressed as in Eq. (4).

$$\text{CEY int.} \equiv \frac{i(E)}{I_0(E)} \dots\dots\dots (4)$$

The purpose of this study was to investigate the difference in the chemical state of carbon depending on the morphology (e.g., bulk or lamellar) of the sample and compare the differences in the chemical state between the surface and bulk using the transmission and CEY methods. In this study, the spectra obtained using the iron *L*-edge and carbon *K*-edge transmission methods, alongside the CEY approach, were investigated. The dwell times for the iron *L*-edge and carbon *K*-edge measurements were 10 ms and 50 ms, respectively.

2.4. First-principles Calculations

To calculate the X-ray absorption spectroscopy (XAS) spectrum, after structural optimization of θ -Fe₃C by density functional theory (DFT) calculations, full-potential multiple scattering theory (FP-MST) computation was performed using the optimized structure. In the DFT calculations, in addition to the typical θ -Fe₃C (i.e., strainless), the XAS spectra of θ -Fe₃C with the *b*-axis extended by 1%, 5%, and 10% were also calculated to verify the effect of lattice strain; these calculations were performed by the projector augmented wave (PAW) method using the Vienna Ab initio Simulation Package (VASP).^{17,18)} The generalized gradient approximation of the Perdew-Burke-Ernzerhof functional (GGA-PBE)¹⁹⁾ was used for the exchange-correlation potential, with a wavefunction cutoff energy of 550 eV. For the reciprocal lattice points, the reciprocal lattice space was divided by the Monkhorst–Pack method²⁰⁾ to obtain a $10 \times 10 \times 10$ mesh. The threshold for structural optimization was calculated when the force acting on each atom was below 0.1 eV/nm.

Based on the above structure, the XAS simulation spectrum was calculated by real space multiple scattering (RSMS). Since a substance was photo-excited in the spectroscopic process, information on the excited-state F_f of the substance, as well as the ground state, was required. In the case of inner-shell excitation spectroscopy, during X-ray absorption, the wavelength (i.e., energy) dependence of the X-ray absorption coefficient can be observed by using the electric dipole approximation and the absorption coefficient $\mu(\omega)$, which can be expressed by the following equation:

$$\mu(\omega) \propto \sum_f |\langle \Psi_f | \epsilon \cdot \mathbf{r} | \Psi_i \rangle|^2 \delta(E_f - E_i - \hbar\omega) \dots\dots\dots (5)$$

where $|\Psi_i\rangle$, E_i , $|\Psi_f\rangle$, and E_f are the ground state and its

energy, alongside the excited state and its energy, respectively. ϵ is the X-ray polarization vector. $|\Psi_f\rangle$ includes a state function that covers the scattering process of photoelectrons in a solid, a screening effect of the inner shell vacancies, and many-body effects such as the exchange-correlation potential. Therefore, using the optical potential Σ^{opt} , which depends on the energy of the photoelectrons, $|\Psi_f\rangle$ can be described as follows:

$$[\nabla^2 + k^2 - V_{Hartree}] \Psi_f(r) = \int \Sigma^{opt}(r, r'; \hbar\omega) \Psi_f(r') dr' \dots\dots (6)$$

In this calculation, the optical potential of the atom was calculated using the one including the imaginary part of the Hedin–Lundqvist (HL) potential.²¹⁾ Meanwhile, the ground-state potential was generated from the superposition of the charge densities of each atom obtained from the HL potential. As for the excited state, the core Hall effect was introduced by transitioning the 1s inner shell electron to the unoccupied state and stabilizing only the valence state, which is called the frozen-core approximation. The excited-state potential obtained by the frozen-core approximation was self-consistently solved only in the atomic-level category and the overall potential was generated from the superposition of the charge densities of each atom obtained thereafter. Since the calculation method dealt with distorted crystal systems, such as orthorhombic crystals, the full-potential real-space multiple-scattering (FP-RSMS) was employed, for which the FPMS package²²⁾ was used. In this method, the potential can be defined in the entire region of the calculation system by dividing the region between the scattering sites by the Voronoi polyhedron. In addition, an empty cell (EC) was introduced to improve the calculation convergence. The radius of the scattering site was 0.14 nm for iron, whereas the radii were 0.1 nm for both carbon and EC. The scattered waves at each scattering site were considered from one to four and the cluster used for the calculation had a radius of 0.8 nm (approximately 300 atoms). These parameters were determined by confirming the convergence of the spectral shape. Moreover, the relative relationship of the energy axes of the calculated spectrum was calibrated by approximating the potential of the surface average to the vacuum level in all systems. Since the lifetime of the carbon *K*-edge excitation process was 0.1 eV (full width at half maximum²³⁾), all calculated spectra were also further broadened with the Lorentz function.

3. Results and Discussion

The TEM image of one thin-film sample is demonstrated in Fig. 5, in which (a)–(d) correspond to the areas of Figs. 2(a)–2(d), respectively. On the other hand, the OD images at 280.0 eV (i.e., the energy before the absorption edge of the carbon *K*-edge) and 285.4 eV, within the white dotted line area in Fig. 5, are illustrated in Figs. 6(a) and 6(b), respectively. Meanwhile, the residual image obtained by subtracting Figs. 6(a) from 6(b) is shown in Fig. 6(c). The images in Fig. 6 were measured at 30 nm/pixel. In Fig. 6(a), a lamellar microstructure was not observed, as confirmed by Fig. 5, whereas a clear pearlite lamellar structure was detected in Fig. 6(b), and the microstructure could be observed clearly in Fig. 6(c). Therefore, the pearlite microstructure with an interval of approximately 100 nm could be identified by the

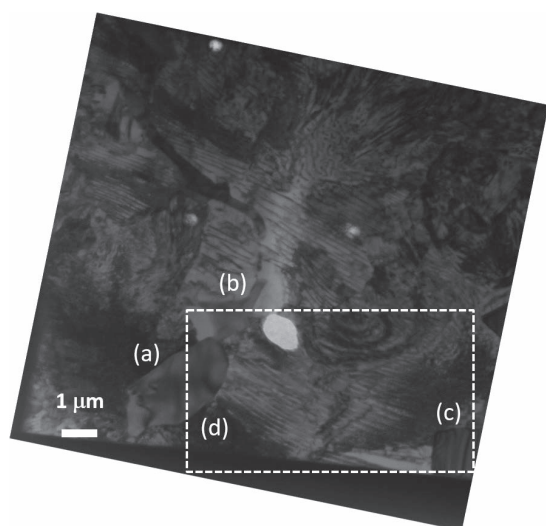


Fig. 5. TEM image of the thin-film sample. (a)–(d) correspond to the areas in Figs. 2(a)–2(d), respectively. The white dotted line indicates the observation area for STXM.

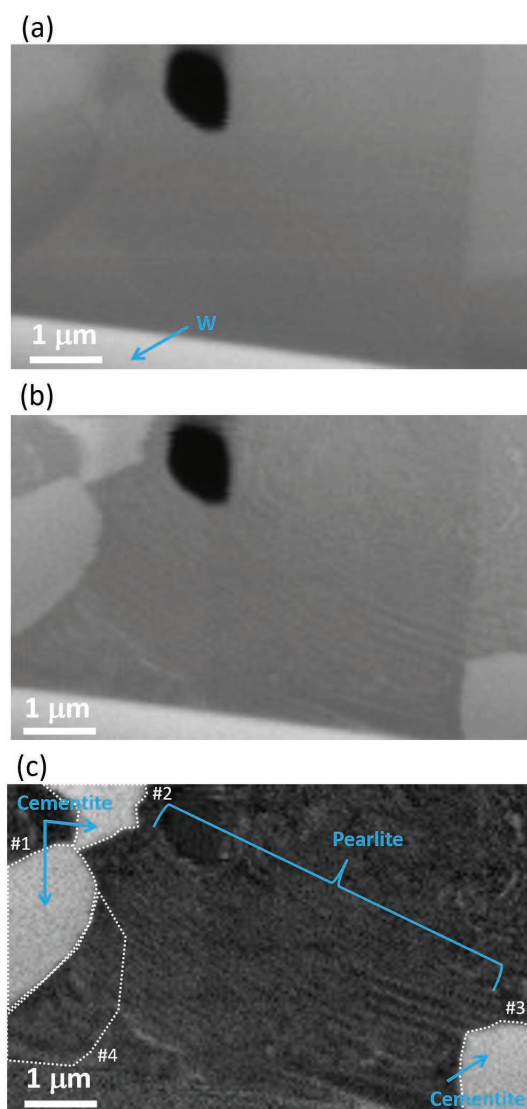


Fig. 6. (a) X-ray absorption image at 280.0 eV (pre-edge), (b) X-ray absorption image at 285.4 eV, and (c) the residual image between (a) and (b). (a)–(c) were measured at 30 nm/pixel. #1–4 shows the areas represented in Figs. 2(a)–2(d), respectively. W in Fig. 2(a) is tungsten for the protective layer for FIB processing. (Online version in color.)

OD contrast at the carbon *K*-edge by STXM. This is the first reported observation of the Fe–C alloy microstructure using X-ray microscopy on the nanometer scale. The contrast of the OD images was affected by the chemical structure of the element. However, it was not sensitive to the crystal orientation and defects, which strongly affected the contrast of the TEM images.

The XAS profiles of grained θ -Fe₃C and the pearlite microstructure measured by the transmission method, together with the surface measured by the CEY method, are shown in **Fig. 7**. The carbon *K*-edge in the areas around #1–4 in Fig. 6(c) by the transmission method and surface of the sample in the CEY method are presented in Fig. 7(a). The spectra in CEY method are originated from the STXM-observed surface of the thin film in both of carbon *K*-edge and iron *L*-edge absorption. These spectra were normalized at 288.2 eV. In the CEY spectrum, there were peaks that originated from the functional groups of hydrocarbons, such as alcohol (approximately 287.0 eV) and aldehyde (approximately 288.0 eV) groups.²⁴ There were no peaks that originated from hydrocarbons; however, there were two broad peaks in the energy range of 283.0–290.0 eV. Similar spectral shape data for carbon *K*-edge absorption were also reported in EELS experiments.⁷ Since the CEY spectrum of the pearlite area was approximately the same as that of the grained θ -Fe₃C area, the carbon *K*-edge spectra of the surface represented the average spectra of the entire surface of the thin-film sample. The OD intensity ratios also varied between grained and lamellar θ -Fe₃C. In the following preliminary examination, to simplify the calculations, it was assumed that all contaminant layers were ethanol and the density was the same as that of liquid (*i.e.*, 0.789 g/cm³, 46.07 g/mol); the thickness of the contamination layer on the sample surface was assumed to be 1 nm. If the real thickness of the contamination layers was much greater than 1 nm, the CEY spectra of iron would not be detected due to the probing depth of the CEY method, which was on the order of a few nanometers.¹⁶ The number of moles of the contamination layer per unit area (n_{con}) was $n_{\text{con}} = 0.789 \times 10^{-7} \text{ g/cm}^2 = 0.171 \times 10^{-8} \text{ mol/cm}^2$, whereas that of the carbon atoms per unit area N_{con} contained in the contamination layer was $N_{\text{con}} = 0.514 \times 10^{15}$. In the same procedure for the pearlite microstructure, the number of moles per unit area was $n_{\text{sam}} = 0.115 \times 0.430 \times 10^{-6} \text{ mol/cm}^2 = 0.495 \times 10^{-7} \text{ mol/cm}^2$, whereas that of the carbon atoms in pearlite steel was $N_{\text{sam}} = 0.745 \times 10^{16}$ (the cementite fraction was 11.5%, which was the equilibrium state of the initial composition of the sample); the sample thickness was approximately 80 nm with a density of 7.73 g/cm³ and molar mass of 179.4 g/mol. The $N_{\text{sam}}/N_{\text{con}}$ ratio was greater than 14. We concluded that the carbon detected in the pearlite microstructure originated from θ -Fe₃C, rather than ferrite, because the amount of carbon as a solid solution element in pearlite was less than 0.01% of the mass in the equilibrium state of the initial sample composition. The absorption spectrum of carbon obtained in the pearlite microstructure largely reflected carbon atoms that were not in the contamination layer but in the pearlite microstructure of the sample instead.

The iron *L*-edge spectra in #1 and #4 in Fig. 6(c), representing the transmission method and surface of the sample

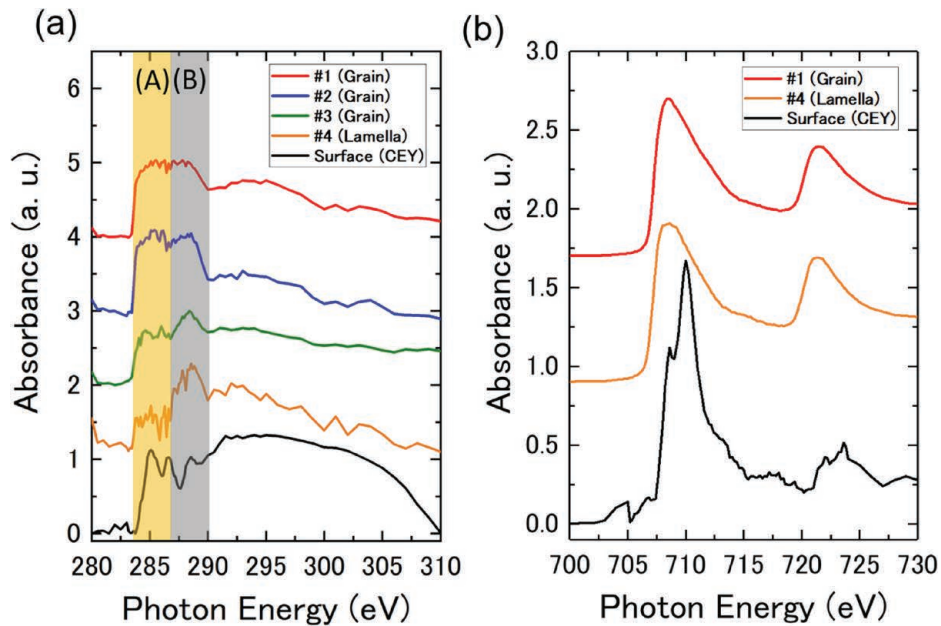


Fig. 7. (a) Carbon *K*-edge spectra in areas #1–4 in Fig. 6(c) for the transmission mode and surface of the sample by the CEY mode, and (b) Iron *L*-edge spectra in areas #1 and #4 in Fig. 6(c) for the transmission mode and surface of the thin film sample by the CEY mode. (Online version in color.)

by the CEY method, which were normalized at 708.0 eV, are shown in Fig. 7(b). Since the CEY spectrum of the pearlite area was approximately the same as that of the grained θ -Fe₃C area, the iron *L*-edge spectra of the surface also reflected the average spectra of the entire surface of the thin film sample. As a preliminary examination for a detailed discussion, the effects of surface oxidation and/or contamination were considered. Comparing the spectra of the pearlite area and the grained θ -Fe₃C area by the transmission method revealed that both ferrite and θ -Fe₃C existed in the spectrum of the pearlite area; hence, the spectrum of the pearlite area had a shoulder on the higher energy side of the peaks at approximately 708.0 eV and 723.0 eV, respectively. Despite some differences in how the tails were pulled, similar behavior was observed. There was approximately no iron oxide in either spectrum. The peak intensity of 710.0 eV by the CEY method was higher than that obtained by the transmission method. Therefore, the surface of the sample was oxidized; however, the influence of surface oxidation was negligible when we considered the spectra using the transmission method.

Moreover, the chemical state of carbon in each microstructure (*i.e.*, grain and lamellar θ -Fe₃C) in the Fe–C alloy was discussed. More than two types of chemical state existed in θ -Fe₃C: (A) $E = 283.0$ – 286.5 eV, and (B) $E = 286.5$ – 290.0 eV, as shown in Fig. 7(a). The ratios of these chemical states were found to be different between grained θ -Fe₃C and lamellar θ -Fe₃C in pearlite. In addition, a difference was observed between the carbon *K*-edge spectra of grained θ -Fe₃C and those of lamellar θ -Fe₃C in pearlite, which may have originated from the microstructure and morphology of θ -Fe₃C.

To confirm whether the carbon *K*-edge spectrum of the pearlite microstructure actually reflected the pearlite microstructure instead of surface contamination, the amounts of carbon on the surface contamination layer and in the pearlite microstructure area were compared. The difference between

Table 2. Lattice parameters and total energy for the first-principles calculations.

| $\Delta b/b$ | 0 | 0.01 | 0.05 | 0.1 |
|-------------------|----------|----------|----------|----------|
| a (nm) | 0.5036 | 0.5036 | 0.5036 | 0.5036 |
| b (nm) | 0.6725 | 0.6791 | 0.7060 | 0.7396 |
| c (nm) | 0.4480 | 0.4480 | 0.4480 | 0.4480 |
| Total energy (eV) | –135.344 | –135.327 | –134.977 | –134.108 |

the spectra of the grained and lamellar θ -Fe₃C in Fig. 7(a) could have originated from the stress and defects generated during the formation of coarse grains of θ -Fe₃C and the lamellar microstructure. Taniyama *et al.*²⁵⁾ and Kosaka *et al.*²⁶⁾ reported that θ -Fe₃C in pearlite was elastically distorted from a few to several percent in the *b*-axis direction.

Therefore, to determine the origins of the difference in the carbon *K*-edge spectra of pearlite and bulk grained θ -Fe₃C, we performed first-principles calculations (*i.e.*, PAW method, VASP) and multiple scattering calculations (full potential method, FPMS). The calculation conditions can be described as follows.

We examined the cases where: (1) the ratio of change $\Delta b/b$ varied (Table 2); and (2) under the assumption that each crystal plane shown in Fig. 8 was irradiated with X-rays. The former corresponds to the stress effect, whereas the latter corresponds to the evaluation of the crystal anisotropy of θ -Fe₃C. In these calculations, the lattice parameters *a* and *c* were fixed.

First, the carbon *K*-edge spectra of θ -Fe₃C were calculated under the four stress conditions listed in Table 2. In these calculations, it was assumed that the calculated system was a single crystal that was irradiated with unpolarized X-rays. The results were the average spectra when X-ray was irradiated from *a*-, *b*-, and *c*-axis, respectively. The results, shown in Fig. 9(a), demonstrated that the peak

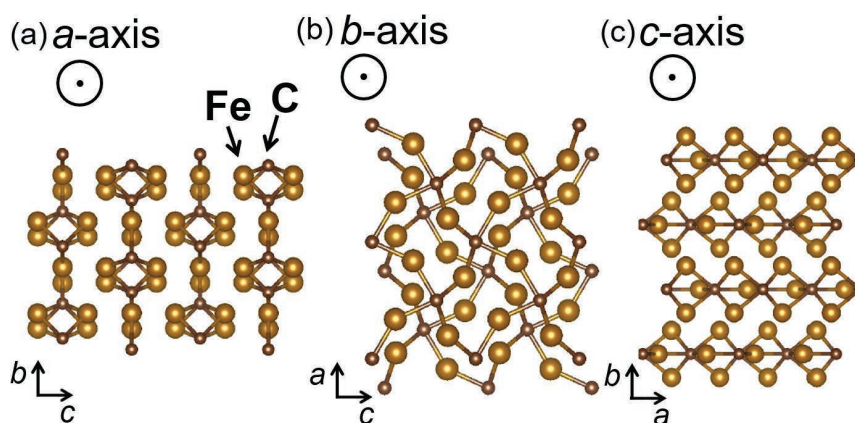


Fig. 8. (a) Crystal structure of θ -Fe₃C as seen from the a -axis, (b) b -axis, and (c) c -axis. (Online version in color.)

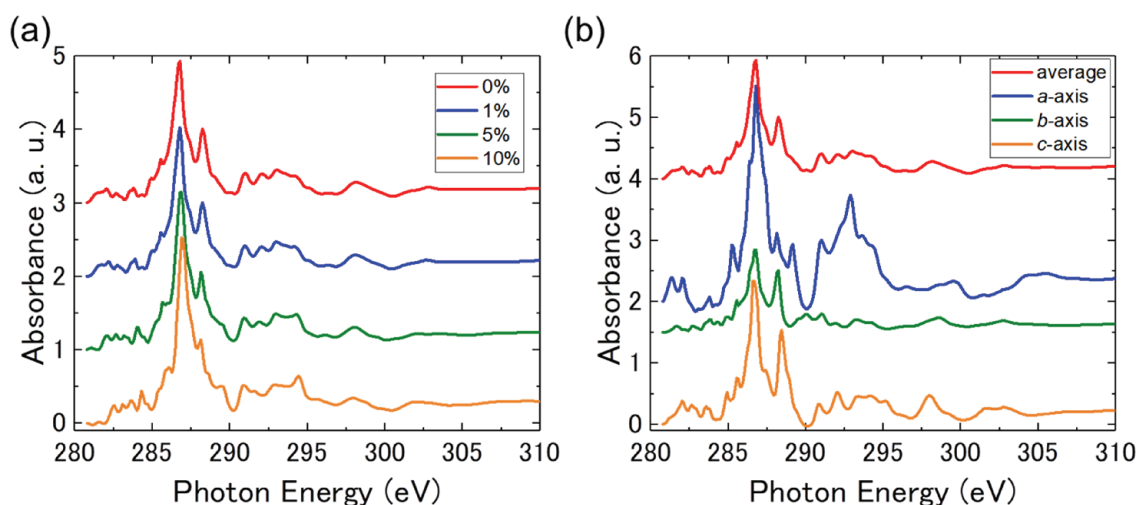


Fig. 9. (a) Carbon K -edge spectra of θ -Fe₃C when the $\Delta b/b$ ratio changed by +0, 1, 5, and 10%; (b) Carbon K -edge spectra assuming that X-rays were irradiated from each direction specified from (a) to (c) in Fig. 8. In calculations (a) and (b), unpolarized X-ray and polarized X-rays were assumed along each axis, respectively. (Online version in color.)

intensity of approximately 288.2 eV decreased with increasing $\Delta b/b$ ratio of change. As shown in Fig. 8(a), the crystal structure of θ -Fe₃C consisted of stacking planes, including carbon atoms along the b -axis, which were located in a triangular prism composed of six iron atoms on each corner of the prism. The expansion of the b -axis was mainly attributed to the distance between the planes, rather than the increase in the triangular prism. Hence, the intensity of the sub peak of approximately 288.2 eV became smaller with increasing intersurface distance; furthermore, bonds related to carbons were located beyond the planes. In other words, it was qualitatively understood that the bonds between the planes not only originated from the bonds of Fe–Fe but also from those of C–C or C–Fe–C. In addition, the intensity of XAS originating from carbon 1s was approximately proportional to the density of states in the unoccupied state of carbon 2p.

According to the calculated spectra, the sub-peak at approximately 288.0 eV that originated from the C–C and C–Fe–C bonds between planes perpendicular to the b -axis was assumed to be weaker compared to the peak at approximately 286.0 eV that originated from the Fe–C bonds on the in-plane perpendicular to the b -axis, representing the main peak. This is because the lattice parameters did not change without also changing the lattice constant of the

b -axis (Fig. 8(b)). Therefore, the bonds on the in-plane were not stronger than those on the planes and were dominated by the metallic bonds originating from Fe–Fe. In addition, as a feature of the Fe–C bond in this system, the bonds between the Fe–C sheets perpendicular to the b -axis were attributed to the peaks on the high-energy side compared to the bonds in the sheet perpendicular to the b -axis; the carbon 2p electrons may have been more strongly bonded between the sheets than in the sheets. These features may have caused the elastic anisotropy of θ -Fe₃C. However, the spectral shape obtained in the experiment could not be reproduced by these calculations because the peak intensity at 285.0 eV was equivalent to the peak intensity at 288.0 eV. As shown by Taniyama *et al.*²⁵⁾ and Kosaka *et al.*,²⁶⁾ the $\Delta b/b$ ratio of θ -Fe₃C in pearlite increased. According to the calculation results, the peak of the grained pearlite at 288.0 eV was expected to be stronger. These calculation results were performed in similar conditions as those reported by Yoshimoto *et al.*⁹⁾ and were consistent with their results.

Second, the carbon K -edge spectrum obtained when assuming X-ray irradiation on each case is illustrated in Fig. 9(b). In these calculations, polarized X-rays were assumed along each axis. Regarding the influence of crystal anisotropy, the peak intensity at approximately 288.0 eV

was sensitive but the difference in the experimental results could not be reproduced. Thus, the observed difference in the chemical structure (*i.e.*, the shape of the carbon *K*-edge spectrum) of the pearlite microstructure and grained θ -Fe₃C could not be explained by only stress or crystal anisotropy. In the future, we will perform calculations that consider crystal defects and discuss the origins of the chemical state of θ -Fe₃C depending on the microstructure. From the Euler angles in Table 1, the coefficients used to express each spectrum in each area in Figs. 2(a)–2(d) can be considered as a linear combination of the spectrum obtained when irradiating with X-rays parallel to each axial direction in Fig. 9(b). These coefficients were calculated as follows: the basis vectors of the Cartesian coordinate system (*i.e.*, (*a* 0 0), (0 *b* 0), (0 0 *c*)) in Fig. 3(a) were rotated by Euler angles (see Table 2) using Eq. (7), where *a*, *b*, and *c* are lattice constants of θ -Fe₃C; the normalized coefficients for the linear combination were normalized coefficients when (0 1 0) (*i.e.*, the direction of linear polarization of X-rays) was expressed by the rotated vectors.

$$\begin{pmatrix} \cos \Phi & -\sin \Phi & 0 \\ \sin \Phi & \cos \Phi & 0 \\ 0 & 0 & 1 \end{pmatrix} \begin{pmatrix} \cos \theta & 0 & \sin \theta \\ 0 & 1 & 0 \\ -\sin \theta & 0 & \cos \theta \end{pmatrix} \begin{pmatrix} 1 & 0 & 0 \\ 0 & \cos \Psi & -\sin \Psi \\ 0 & \sin \Psi & \cos \Psi \end{pmatrix} = \begin{pmatrix} \cos \theta \cos \Psi & \sin \Phi \sin \theta \cos \Psi - \cos \Phi \sin \Psi & \cos \Phi \sin \theta \cos \Psi + \sin \Phi \sin \Psi \\ \cos \theta \sin \Psi & \sin \Phi \sin \theta \sin \Psi + \cos \Phi \cos \Psi & \cos \Phi \sin \theta \sin \Psi - \sin \Phi \cos \Psi \\ -\sin \theta & \sin \Phi \cos \theta & \cos \Phi \cos \theta \end{pmatrix} \quad (7)$$

These normalized coefficients are presented in Table 3. The experimental spectra in Fig. 7(a) and calculated spectra using these coefficients are illustrated in Fig. 10. Even considering the strain in the *b*-axis direction and the crystal-line anisotropy of θ -Fe₃C, the carbon *K*-edge spectra of the experiment could not be reproduced by calculations. It was presumed that other factors, such as lattice defects, could not be considered in these calculations because the calculation results were consistent with the results of Yoshimoto *et al.*⁹⁾ Based on these experiments, the difference in the spectral shape indicated the chemical state of carbon variations due to the difference in the morphology of the same θ -Fe₃C; however, the origin of this difference could not be clearly explained.

Nevertheless, the results of the experiments and calculations reported above suggest the following: there was a difference in the intensity ratio originating from the Fe–C bonds both in-plane (at 286.0 eV) and out-of-plane (at 288.0 eV) parallel to the *b*-axis, depending on the microstructure (either grain or lamella). In other words, the Fe–C bonds of the in-plane in the lamellar microstructures were weaker than those in the grains. In the process of microstructure formation, the distribution of the local carbon content varied depending on the morphology, following a known partitioning phenomenon,²⁷⁾ suggesting that the detailed crystal structure, such as in terms of the site occupancies of carbon, may have varied. In this study, only one field of view was observed for the lamellar microstructure; therefore, in the future, the number of observed fields of view will be increased to verify the above information.

Table 3. Normalized coefficients of the unit cell vectors after Euler angle rotation to express the unit vector of the *b*-axis (010) (parallel to the electric field vector of the X-ray).

| | <i>C_a</i> (<i>a</i> -axis) | <i>C_b</i> (<i>b</i> -axis) | <i>C_c</i> (<i>c</i> -axis) |
|----|--|--|--|
| #1 | 0.87 | 0.31 | 0.38 |
| #2 | 0.89 | 0.44 | 0.13 |
| #3 | 0.91 | 0.26 | 0.33 |
| #4 | 0.50 | 0.24 | 0.83 |

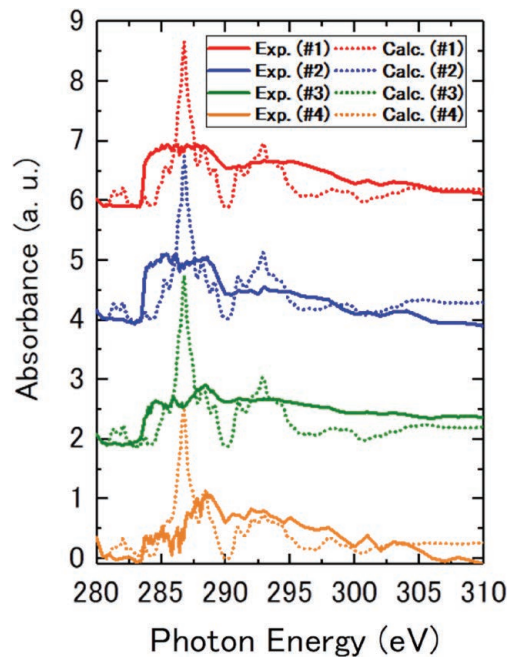


Fig. 10. (Solid line) Measured carbon *K*-edge spectra by STXM same as those of #1–4 in Fig. 7(a), (Dotted line) Calculated carbon *K*-edge spectra (without stress) of θ -Fe₃C in each crystal orientation of #1–4 in Fig. 2. (Online version in color.)

4. Conclusion

To investigate the chemical state of an additional element, *i.e.*, carbon in steel, we first verified whether the microstructure of steel could be identified using STXM. We successfully identified grained θ -Fe₃C and pearlite structures (with a lamellar spacing of approximately 100 nm) in an Fe–C alloy using carbon *K*-edge absorption. In addition, the possibility of the extraction of the XAS spectrum of a specific element at a specific location with a spatial resolution of approximately 50 nm by STXM was confirmed.

Moreover, to compare the difference in the average information on the surface and bulk, alongside the difference in the chemical state of the carbon in θ -Fe₃C depending on the morphology (*i.e.*, grains or lamellar), we applied the transmission and CEY methods simultaneously to perform two-dimensional chemical state mapping of the surface (thickness on the order of a few nanometers) and bulk (thickness of approximately 80 nm) in the Fe–C alloy. A clear difference was found between the chemical states of carbon of the grained θ -Fe₃C and pearlite microstructures of the Fe–C alloy. The spectra obtained by the transmission

method originated from carbon in the sample.

Finally, to examine the origin of this difference, we performed first-principles calculations by considering the stress in the *b*-axis direction and crystal anisotropy, which could not reproduce the experimental spectra based on crystal structure models that have been reported. In the future, we will perform calculations that consider not only the strain and crystal anisotropy but also other factors (*e.g.*, the detailed crystal structure, such as the site occupancies of carbon), and consider the origins of the difference in the chemical state of carbon in θ -Fe₃C depending on the microstructure.

In terms of the development of the STXM instrument, the air exposure system enabled the reduction of the contamination of the sample to investigate a lower amount of carbon as a solid solution element in materials such as ferrite and martensite. Using this system, we were able to study the relationship between the distribution of composition and the chemical state of carbon, alongside that of the strain in the grains of θ -Fe₃C. This cannot be achieved by conventional techniques, such as TEM. Generally, the spatial distributions of the elements and microstructures were mainly investigated by APT and TEM. However, when it was essential to consider carbides, which did not possess a crystal structure that melted during the heat treatment or a chemical bond between Fe and carbon at the grain boundary, the investigations of the conventional microstructure and crystal structure were insufficient to identify the essential role of carbon in their mechanical properties. Therefore, it was important to analyze the chemical states of carbon in steel (a common structural material) on the nanoscale, which is a general method for functional materials. Regarding the analysis of the chemical structure, the same discussion could be applied to other additive elements in steel.

Acknowledgement

We would like to thank Mr. Michiaki Matsumoto (Nippon Steel Technology Co. Ltd.) for useful discussions and support on the manufacturing process of thin film samples. The technical advice and support received from Prof. Kazuhiko Mase at BL-13A (KEK) is also gratefully acknowledged. The experiment was conducted by the approval of the Photon Factory Program Advisory Committee (proposal nos. 2015C206 and 2019C202). In this paper, we also used the findings obtained from the experiments in BL-19A in KEK-PF as references for consideration.

REFERENCES

- 1) E. C. Bain and H. W. Paxton: *Alloying Elements in Steel*, Chapman and Hall, London, (1962), 59.
- 2) E. Courtois, T. Epicier and C. Scott: *Micron*, **37** (2006), 492. <https://doi.org/10.1016/j.micron.2005.10.009>
- 3) T. Yamashita, Y. Tanaka, M. Nagoshi and K. Ishida: *Sci. Rep.*, **6** (2016), 29825. <https://doi.org/10.1038/srep29825>
- 4) C. Zhu, A. Cerezo and G. D. W. Smith: *Ultramicroscopy*, **109** (2009), 545. <https://doi.org/10.1016/j.ultramic.2008.12.007>
- 5) Y. Kobayashi, J. Takahashi and K. Kawakami: *CAMP-ISIJ*, **28** (2015), 307, CD-ROM (in Japanese).
- 6) A. J. Scott, R. Brydson, M. MacKenzie and A. J. Craven: *Phys. Rev. B*, **63** (2001), 245105. <https://doi.org/10.1103/PhysRevB.63.245105>
- 7) K. He, A. Brown, R. Brydson and D. V. Edmonds: *J. Mater. Sci.*, **41** (2006), 5235. <https://doi.org/10.1007/s10853-006-0588-4>
- 8) K. Ninomiya, K. Kamitani, Y. Tamenori, K. Tsuruta, T. Okajima, D. Yoshimura, H. Sawada, K. Kinoshita and M. Nishibori: *Tetsu-to-Hagane*, **104** (2018), 628 (in Japanese). <https://doi.org/10.2355/tetsutohagane.TETSU-2018-050>
- 9) Y. Yoshimoto, M. Yonemura, S. Takakura and M. Nakatake: *Metall. Mater. Trans. A*, **50** (2019), 4435. <https://doi.org/10.1007/s11661-019-05328-4>
- 10) G. F. Bastin and H. J. M. Heijligers: *X-Ray Spectrom.*, **15** (1986), 135. <https://doi.org/10.1002/xrs.1300150212>
- 11) W. Lengauer, J. Bauer, M. Bohn, H. Wiesenberger and P. Ettmayer: *Microchim. Acta*, **126** (1997), 279. <https://doi.org/10.1007/BF01242334>
- 12) J. B. Seol, G. H. Gu, N. S. Lim, S. Das and C. G. Park: *Ultramicroscopy*, **110** (2010), 783. <https://doi.org/10.1016/j.ultramic.2009.12.006>
- 13) N. V. Smith: *Rep. Prog. Phys.*, **51** (1988), 1227. https://doi.org/10.1007/978-1-4684-6021-6_27
- 14) Y. Takeichi, N. Inami, H. Suga, C. Miyamoto, T. Ueno, K. Mase, Y. Takahashi and K. Ono: *Rev. Sci. Instrum.*, **87** (2016), 013704. <https://doi.org/10.1063/1.4940409>
- 15) J. Stöhr: *NEXAFS Spectroscopy*, Springer-Verlag, Berlin Heidelberg, (1992), 114. <https://doi.org/10.1007/978-3-662-02853-7>
- 16) J. Als-Nielsen and D. McMorrow: *Elements of Modern X-ray Physics*, John Wiley and Sons, New York, (2001), 239.
- 17) G. Kresse and J. Furthmüller: *Comput. Mater. Sci.*, **6** (1996), 15. [https://doi.org/10.1016/0927-0256\(96\)00008-0](https://doi.org/10.1016/0927-0256(96)00008-0)
- 18) P. Blöchl: *Phys. Rev. B*, **50** (1994), 17953. <https://doi.org/10.1103/PhysRevB.50.17953>
- 19) J. P. Perdew, K. Burke and M. Ernzerhof: *Phys. Rev. Lett.*, **77** (1996), 3865. <https://doi.org/10.1103/PhysRevLett.77.3865>
- 20) H. J. Monkhorst and J. D. Pack: *Phys. Rev. B*, **13** (1976), 5188. <https://doi.org/10.1103/PhysRevB.13.5188>
- 21) L. Hedin: *Phys. Rev.*, **139** (1965), A796. <https://doi.org/10.1103/PhysRev.139.A796>
- 22) K. Hatada, K. Hayakawa, M. Benfatto and C. R. Natoli: *Phys. Rev. B*, **76** (2007), 060102(R). <https://doi.org/10.1103/PhysRevB.76.060102>
- 23) M. O. Krause and J. H. Oliver: *J. Phys. Chem. Ref. Data*, **8** (1979), 329. <https://doi.org/10.1063/1.555595>
- 24) G. D. Cody, H. Ade, C. M. O'D. Alexander, T. Araki, A. Butterworth, H. Fleckenstein, G. Flynn, M. K. Gilles, C. Jacobsen, A. L. D. Kilcoyne, K. Messenger, S. A. Sandford, T. Tylliszczak, A. J. Westphal, S. Wirick and H. Yabuta: *Meteorit. Planet. Sci.*, **43** (2008), 353. <https://doi.org/10.1111/j.1945-5100.2008.tb00627.x>
- 25) A. Taniyama, T. Takayama, M. Arai and T. Hamada: *Metall. Mater. Trans. A*, **48** (2017), 4821. <https://doi.org/10.1007/s11661-017-4229-0>
- 26) M. Kosaka, K. Ushioda, T. Teshima, M. Nishida and S. Hata: *ISIJ Int.*, (2021), (Advance Publication). <https://doi.org/10.2355/isijinternational.ISIJINT-2021-194>
- 27) J. Speer, D. K. Matlock, B. C. De Cooman and J. G. Schroth: *Acta Mater.*, **51** (2003), 2611. [https://doi.org/10.1016/S1359-6454\(03\)00059-4](https://doi.org/10.1016/S1359-6454(03)00059-4)